Heat treatment effects on Inconel 625 components fabricated by wire + arc additively manufacturing (WAAM)—part 2: mechanical properties

A. N. M. Tanvir[1] · MD R. U. Ahsan[1] · Gijeong Seo[1] · Jae-duk Kim[2] · Changwook Ji[2] · Brian Bates[3] · Yousub Lee[4] · Duck Bong Kim[5]

Abstract

This study investigates the mechanical properties of the wire + arc additively manufactured Inconel 625 thin wall. The first part of this study focused on the microstructural features of the material after time-based annealing. This second part discusses the tensile strength and microhardness of the material after the same annealing procedure (980 °C, hold time 30 min, 1 h, and 2 h). It is found that the annealing procedure improved the ultimate tensile strength by 5%. Although the yield strength remains unchanged up to 1-h of annealing, it increases after 2-h of heat treatment. The presence of strengthening elements and precipitation of secondary phases seem to control the tensile strength of the additively manufactured Inconel 625. On the other hand, the average microhardness does not show any significant trend for time-based heat treatment. However, the layer-specific variation of microhardness was observed in the sample, which may have caused high standard deviation in the as-deposited sample. Overall, the annealing procedure with a 2-h hold time presents the best mechanical properties of the Inconel 625 so far. Nevertheless, further improvement in strength and hardness may require a comprehensive study with location-specific microstructure and mechanical properties analysis before and after the heat treatment procedure.

Keywords Metal additive manufacturing · Wire + arc additive manufacturing · Inconel 625 · Heat treatment · Mechanical property evolution

1 Introduction

Inconel 625 is a nickel-based superalloy, popular for its benefits of high load-bearing capacity, applicability at extremely elevated temperatures, and extraordinary corrosion resistance [1, 2]. These unique properties make its application possible

✉ Duck Bong Kim
  dkim@tntech.edu

1 Department of Mechanical Engineering, Tennessee Technological University, Cookeville, TN 38505, USA

2 Advanced Forming Process R&D Group, Korea Institute of Industrial Technology, Ulsan, Republic of Korea 44413

3 Center for Manufacturing Research, Tennessee Technological University, Cookeville, TN 38505, USA

4 Manufacturing Demonstration Facility, Oak Ridge National Laboratory, Oak Ridge, TN 37830, USA

5 Department of Manufacturing and Engineering Technology, Tennessee Technological University, Cookeville, TN 38505, USA

to critical industrial scenarios. To reduce the material wastage for valuable materials like Inconel, additive manufacturing can be highly beneficial. There are several already commercialized techniques for additive manufacturing of Inconel based on powder feedstock, such as laser powder bed fusion and selective laser melting [3, 4]. However, for fabricating large-sized parts, these processes have some areas to improve, such as powder processing, high cost of powder materials, low deposition rate [5], low energy efficiency, and low fatigue life due to possibility of pores in large-scale parts [6]. Powder-fed directed energy deposition (DED) provides good alternatives to the powder bed technologies in terms of build rate and size. However, even with improved nozzle design, the powder feeding system still experiences a loss of 25% powder [7] which increases the final cost of the product. On the other hand, wire-fed arc-based additive manufacturing techniques can be a possible solution in this circumstance due to its prospect in fabricating a pore-free large-scale structure with a high deposition rate and almost no loss of raw materials.

Wire + arc additive manufacturing (WAAM) using cold metal transfer (CMT) technology is in its early stages of development. This method uses a CMT power supply to melt a solid wire and a robotic or computer numerically controlled (CNC) system for conforming to the desired shape. A CMT system offers high energy efficiency and low spatter when maintaining improved weld bead quality to other gas metal arc welding methods [8–11]. Thus, the fabrication of large-sized parts using this technique can be highly beneficial regarding efficiency in energy and optimizing material wastage while maintaining better part quality. Therefore, several researchers have investigated WAAM of Inconel 625 [12–18]. However, it is very difficult to find out studies that used the CMT-WAAM technique for additive manufacturing of Inconel 625 and further improvement of its properties. This paper is the second part of an effort to improve the metallurgical characteristics of Inconel 625 thin wall fabricated using the CMT-WAAM technique. The first part of this research presented the microstructural features of the material in as-deposited and heat-treated conditions [19]. This next part will discuss the effect of microstructural transformation on the mechanical properties (i.e., tensile strength and hardness) of the material.

Inconel 625 falls in the category of solid solution strengthened superalloys [2]. The unique sustainability of this material at critical environments comes from the strengthening of its Ni-Cr matrix by a solid solution of Nb and Mo [20]. The amount of solid solution strengthening elements highly controls the mechanical properties for this superalloy [21]. However, precipitation of secondary phases such as the Laves phase, δ phase, and metal carbides (MC, M_6C, $M_{23}C_6$) which were formed due to melting, remelting, or heat treatment [22] can also influence the mechanical performance of the Inconel 625 favorably [1, 23] or unfavorably [14, 24, 25]. Among them, the Laves and MC carbides can be formed just after solidification of the weld metal [26–28]. Formation of the Laves may deteriorate the mechanical strength of the material by locally depleting the solid solution strengthening elements (Nb, Mo) from the Ni-Cr matrix [22] and subsequently acting like a crack nucleation zone [14]. On the other hand, MC carbides located at grain boundaries can strengthen the material by transforming the grain boundary to a zigzag shape during solidification [1]. Nevertheless, the overall strength is found to be deteriorated due to containing Laves phases [14, 22, 29]. Standard annealing procedure at 980 °C usually recrystallizes the secondary phases of the material by transforming Laves particles [30]. However, another secondary phase-delta (δ) can be formed for long-term exposure at high temperature during annealing [23]. The formation of this phase can be detrimental to the ductility [31] of the material but is believed to increase overall tensile strength [32] and hardness [31]. The improvement of the tensile strength of Inconel 625 due to the precipitation of the δ phase is related to the slip system of the material. The plate-like δ particles inhibit cross-slip between the dislocation substructures. As a consequence, tensile strength

increases significantly for materials having a high percentage of δ phases [32].

Therefore, heat treatment can significantly improve the mechanical characteristics of Inconel 625 by recrystallization of the secondary phases. A well-researched heat-treating guideline addressing several issues, such as stress-relieving effect on built parts and step-by-step recrystallization process with time-temperature dependence should be adopted. For additively manufactured Inconel 625 parts, several researchers have studied the effect of heat treatment. Xu et al. investigated the microstructure and mechanical properties of Inconel 625 samples fabricated by the pulsed plasma arc deposition (PPAD) method by incorporating three steps of heat treatment. They found that Laves phases in the as-built condition have been completely dissolved after homogenization heat treatment at 1080 °C [15–17]. Marchese et al. did extensive work on heat treatment of additive manufacturing of Inconel 625 samples fabricated using the laser powder bed fusion (L-PBF) method by studying 28 conditions of heat treatment in total. They found improved tensile strength for direct aging at different temperatures and hold time but at the expense of ductility lower than the required minimum [33]. Fang et al. tried to characterize texture and grain boundary of Inconel 625 fabricated by the selective laser melting (SLM) process after heat treatment for stress relieving (870 °C), annealing (980 °C), and complete recrystallization annealing (1150 °C) [34, 35]. Cardozo et al. used the same procedure of heat treatment obtained by Xu et al. (F. Xu, Lv, Liu, Xu, et al., 2013) to see the difference in the mechanical and microstructural properties of Inconel 625, deposited by plasma transferred arc (PTA) method for using two different feedstocks (powder and wire). Secondary δ phases observed to be formed after heat treatment for both powder and wire cases following a decline of hardness in their study [12]. Laser-aided directed metal deposition (DMD) with Inconel 625 was investigated by Dinda et al., emphasizing on the thermal stability of the dendritic morphology of the material under several annealing procedures [36].

In brief, numbers of heat treatment practices have been already investigated for additively manufactured Inconel 625. However, to our knowledge, heat treatment of Inconel 625 manufactured by CMT-based WAAM is still unexplored by the researchers. This study tries to fill up this knowledge gap emphasizing more on property-microstructure correlation after heat treating. The outcome of this study may be used to build a complete heat-treating guideline for Inconel 625 fabricated using the CMT-WAAM system.

2 Experimental procedure

The square wall fabricated during part 1 of this study is used here for further study of the strength of this material [19]. In the previous study, the separated three of the square walls were heat-treated at 980 °C with varying time (i.e., 30 min,

1 h, and 2 h), followed by water quenching [19]. The as-deposited one wall and the three heat-treated walls are then machined down to separate four tensile samples using wire electrical discharge machining from each of the walls as shown in Fig. 1a. ASTM E8 standard for subsidized sample dimension is followed during machining (Fig. 1b). To remove stress concentration due to electrical discharge machining (EDM) cut, the tensile samples are polished with 100 grit polishing cloth afterward. The tensile test was conducted at room temperature in an MTS servo-hydraulic machine with a 3-mm/min strain rate.

The images of the fractured surface were taken with Hitachi SU8020 and Quanta FEI 200 scanning electron microscopes (SEM). The energy dispersive spectroscopy (EDS) was performed with the energy-dispersive X-ray spectroscopy (EDAx) equipped with the SEM. For measurement of microhardness, a Micromet-II microhardness tester with diamond indentation was used, with a force parameter of 500 gf and a 10-s hold time. A Nikon Epiphot-II inverted microscope was used for the evaluation of the microhardness for the different microstructures involved.

3 Results

3.1 Mechanical strength

As the microstructural parts are already discussed in part 1 of this study [19], only the mechanical properties will be presented and analyzed in this part. The sample-specific tensile result is shown in Table 1. The difference in tensile strength and

elongation for different samples designates a high location-based anisotropy for all the heat treatment conditions. Still, the tensile results are averaged to plot in a binary graph of strength and elongation vs. heat treatment conditions plot, as shown in Fig. 2a. The average values of tensile strength are compared with the original dataset for each heat-treating condition to find the best match of the tensile test result to plot engineering stress vs. strain curve. The ultimate tensile strength (UTS) increases proportionally with the heat-treating hold time. However, the yield strength (YS) decreases for 30 min and 1-h heat-treating hold time. However, a substantial increase in YS is found for the 2-h hold time. The elongation (%El) also follows the same path as YS. However, for 1-h heat treatment, the ductility decreases more than the 30-min heat treatment. The mechanism of this behavior of UTS, YS, and %El will be discussed later in this study.

3.2 Microhardness

The measurement of microhardness of the Inconel 625 parts was carried out in three ways: microhardness along the (1) longitudinal (y-axis) direction, (2) longitudinal in a single layer, and (3) transverse (x-axis) direction. Figure 3 a–c schematically describes how the microhardness is measured for all the cases. Figure 4 presents the result of the microhardness for longitudinal and transverse directions. The overall transverse and longitudinal microhardness do not show any significant trend; see Fig. 4a–b). The microhardness seems to vary in a range (220–240 VHN approximately) without following any trend (increasing or decreasing). The anisotropic microstructure even after heat treatment found in previous studies can cause this

Fig. 1 Tensile sample dimensions and locations for cutting

A = 10 mm
B = 30 mm
C = 32 mm
D = R6 mm
E = 3 mm
F = 6 mm
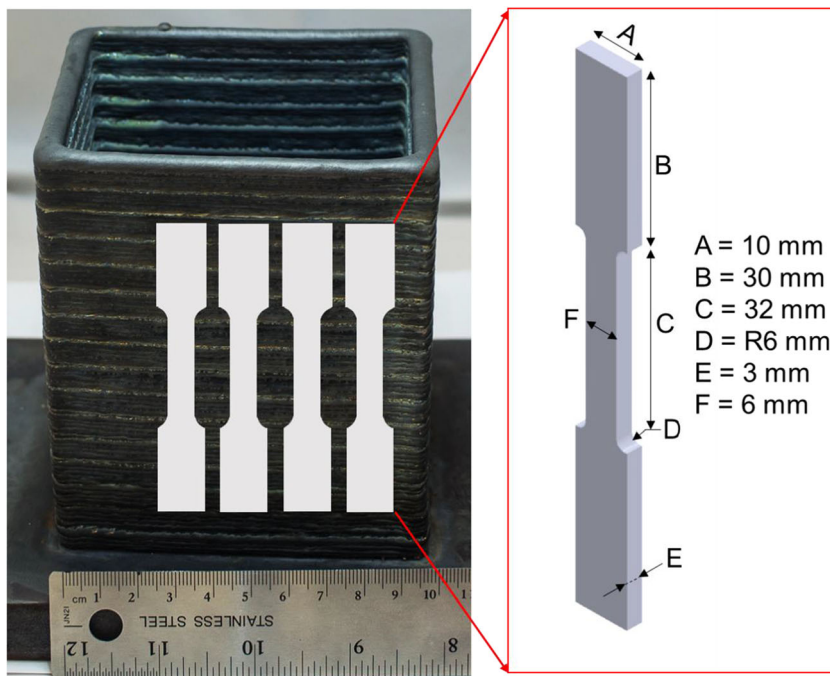
Table 1 Tensile test result for different heat treatment conditions

Heat treatment conditions	Sample no	Tensile strength, σ_u (MPa)	$\sigma_{u,avg}$ (MPa)	Yield strength, σ_y (MPa)	$\sigma_{y,avg}$ (MPa)	Elongation (%)	Average elongation (%)
As-deposited	1	660	658 ± 4	377	373 ± 5	52	56 ± 4
	2	660		377		59	
	3*	658		372		58	
	4	652		367		53	
30-min heat treated	1	677	669 ± 7	365	363 ± 10	50	48 ± 2
	2*	664		369		49	
	3	674		371		45	
	4	660		345		48	
1-h heat treated	1	668	672 ± 8	360	360 ± 11	45	43 ± 1
	2	685		378		43	
	3*	670		353		42	
	4	664		348		43	
2-h heat treated	1	682	688 ± 4	408	397 ± 15	41	46 ± 3
	2*	690		377		50	
	3	689		414		46	
	4	690		390		47	

*Nearest to the average tensile strength. Plotted in Fig. 2b

behavior. However, a more rigorous study tracking microhardness and microstructural phases in a single image is needed to understand this behavior. Also, for the longitudinal case, the standard deviation of the average hardness seems to be decreased gradually for the increased heat-treating hold time. A preliminary study (case 2 measurement) suggests the interface of two layers showing higher hardness in an as-deposited condition and may get relieved due to heat treatment (Fig. 5).

3.3 Fracture analysis

Figure 6 shows the fractured surfaces of the tensile test performed. The fractured surfaces were analyzed under SEM to investigate the fracture mode. Figures 7–12 show the fracture surface analysis for the as-deposited and heat-treated conditions.

3.3.1 As-deposited

The fractography result of the as-deposited sample of Inconel 625 is shown in Fig. 7. The overall fractured surface (Fig. 7a) seems to consist of shear lip and fibrous regions only, due to the inherently ductile nature of the material [31]. The surface also consists of river-like patterns at the lower part of the fractured surface (Fig. 7a). These patterns designate that the crack nucleates from the bottom of the shown fractograph.
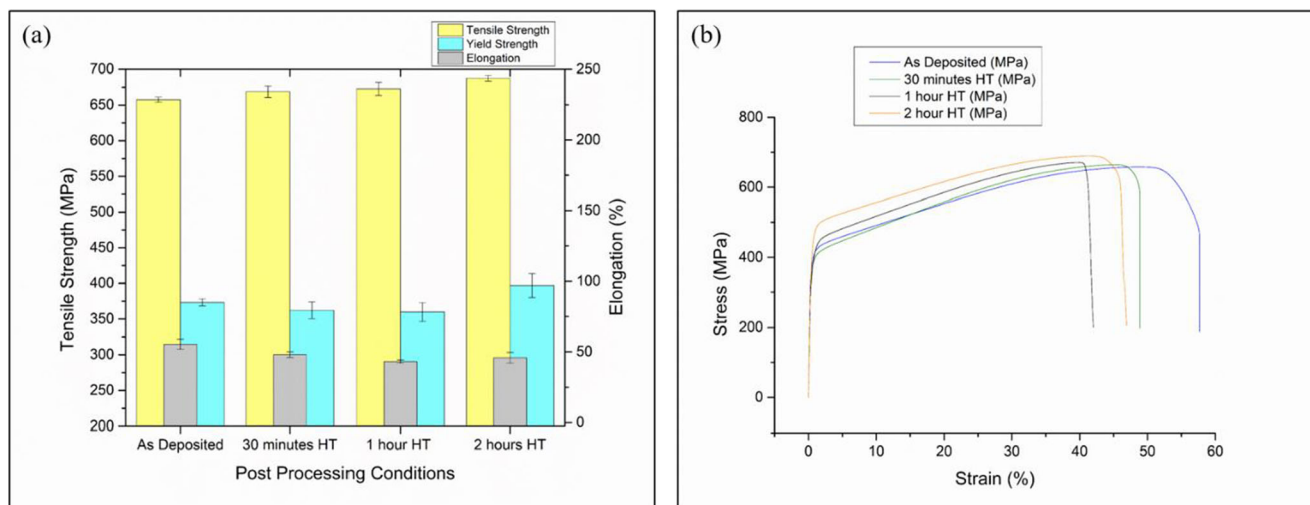
Fig. 2 **a** Tensile strength, yield strength, and elongation evolution depending on post-processing conditions. **b** Engineering stress vs. engineering strain [37]
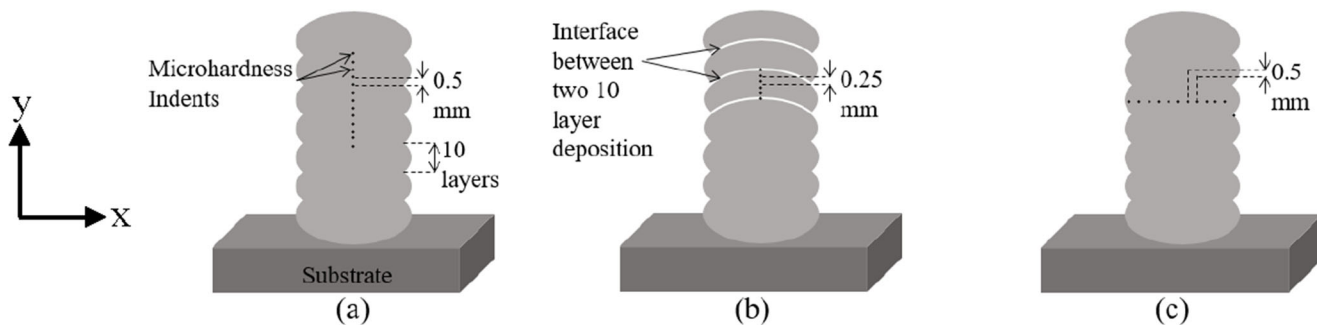
Fig. 3 Microhardness measurement procedure. **a** Longitudinal (*y*-direction) 0.5-mm interval. **b** Longitudinal (*y*-direction) between 10 layers with 0.25-mm interval. **c** Transverse (*x*-direction)

The top right corner of the overall fractured surface (spot 1 Fig. 7a) is dominated by dimple structures, well organized in a narrow path. Between the two narrow paths, a darker zone, with the oval shape of dimples, can be observed (arrows of Fig. 7c). This shape has a well-identified boundary and does not show any crack nucleus or striations, rather a flat fractured surface. The same shapes with dark color tones can also be seen in Fig. 7d. Spot analysis on these spots shows that they contain more Nb and C when compared with the typical wire and Ni-Cr matrix composition. Now, going back to the microstructure analysis of the first part of this research [19], the as-deposited microstructure contained interdendritic spaces filled with secondary Laves phases, as well as low concentration of Ni-Cr matrix. This may have made the interdendritic spaces less strong to the deformation. Furthermore, the dark dimples are comparatively bigger from the dimples adjacent to the brighter zone. Thus, it is evident that these parts showed less resistance to the fracture, which resulted in larger dimples at the fracture zone. The dark color may be due to the lower height of the location of the dimples. Therefore, it can be reasonably assumed that the darker parts can be the less ductile detrimental phases (NbC or Laves) found during microstructural analysis. Some microvoids are also detected in the

same micrograph for the middle region (Fig. 7d). However, they were not observed in the previous microstructural study. The presence of secondary phases may also influence the formation of voids during ductile failure [38]. The middle region also contains a dimple structure that confirms ductile transgranular type fracture occurred during the tensile test.

3.3.2 30 min heat-treated

Figure 8 represents the fracture surface characteristics due to the heat treatment for 30 min of hold time. The fracture again seems to be of a transgranular type resembling the as-deposited sample. However, deep cracks are visible on the fractographs (Fig. 8b). Magnifying more on the crack (Fig. 8c) reveals a high energy slip band created at the top side of the crack. This specific pattern designates the cross-over of grain boundaries. Microvoids are seen over the fractured surface. Some of them are also arranged in an array as shown in Fig. 8d, which causes an elliptical-shaped dimple in the fractured surface. The dark-colored dimples are also observed in the fractured surface similar to the as-deposited sample; see Fig. 8e–f. The bigger dimples also sometimes contain block-shaped particles inside them, which resemble the shape of Ti-
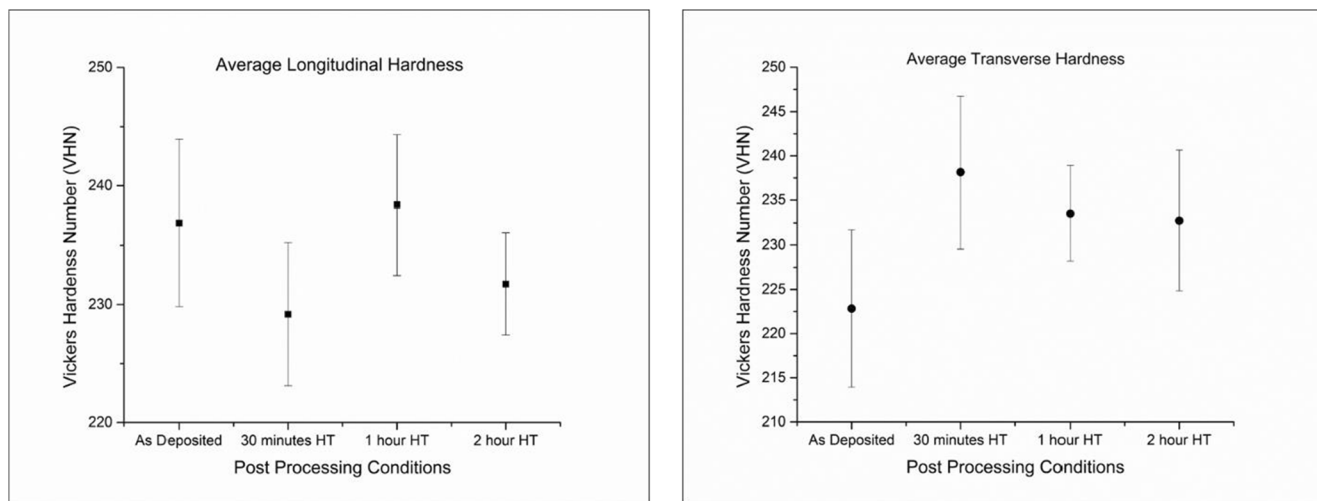
Fig. 4 **a** Average longitudinal microhardness with standard deviation for different post-processing conditions. **b** Average transverse microhardness with standard deviation for different post-processing conditions [37]
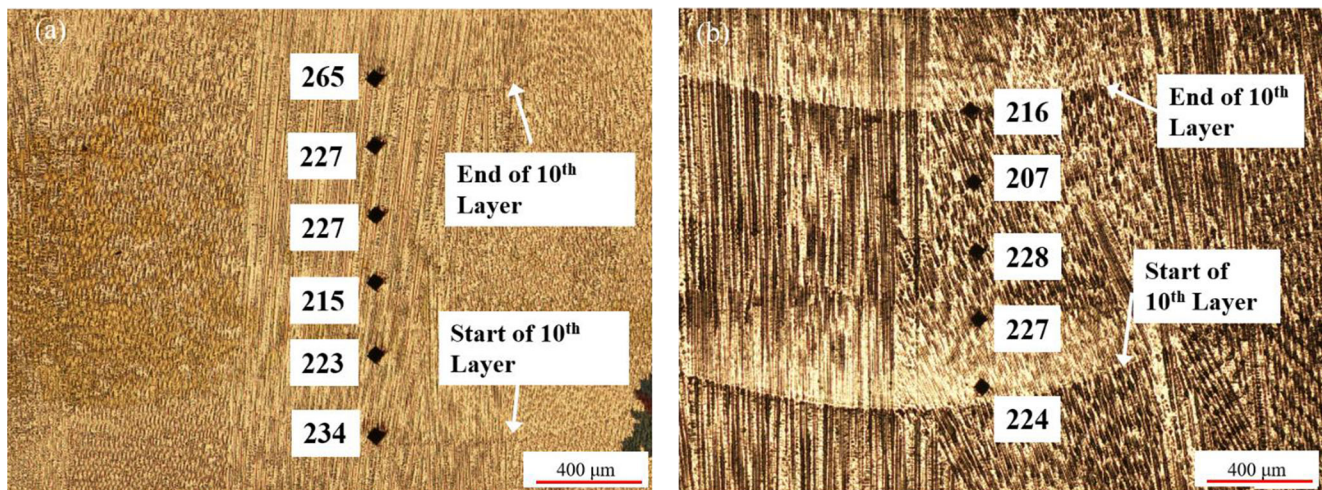
Fig. 5 Microhardness of an (**a**) as-deposited sample and a (**b**) 2-h heat-treated sample

based MC carbide as found in the first part of this research [19].

3.3.3 1-h heat-treated

The shear lip and the final fracture zone designate predominantly ductile failure (Fig. 9a). The right corner region contains disconnected dimples (spot 1—Fig. 9b). Going toward the negative x-direction changes the disconnected morphology to the connected transgranular nature of the dimples (Fig. 9b–e). However, the disconnected morphology of the dimples may be correlated to the dendrites found in the microstructural study [19]. A thick crack associated with river patterns in Fig. 9c denotes high energy fracture in that region. Some smooth-shaped inclusions in the fractograph (Fig. 9d) designates brittle fracture characteristics. EDS spot analysis could not identify these inclusions to be of any different phases. In Fig. 9d, a circular cross-section of a column or sphere-like shape can be identified. This shape has shown an isolated fracture boundary with a separate fracture nucleus. EDS spot and line analysis were carried out on this shape to identify it. The compositional

Fig. 6 Fracture location of the samples at different conditions

analysis on this spot was similar to the typical wire composition and Ni-Cr matrix [19]; see the table in Fig. 10. The line analysis also did not show any anomalies with the surrounding phases of the unidentified object, only showing an isolated characteristic by being surrounded with a boundary (see 301 Fig. 10).

The line and spot analysis in conjunction represent that this object can be due to the isolation of any phase of this microstructure from the surrounding phases. On the other hand, as-deposited and heat-treated microstructure both contained elongated dendrites at different locations. These dendrites were found in a group covering multiple weld layers in some cases [19]. Therefore, it can be reasonably assumed that this specific and separate fracture can be due to the failure of the group of dendrites in isolation from the surrounding matrix. However, this assumption requires further investigation to validate.

3.3.4 2-h heat-treated

The overall fracture surface represents similar characteristics of predominant ductile failure like other of heat-treated and as-deposited cases (Fig. 11a). Several granular thick cracks are observed on the fractured surface (arrows in Fig. 11b). The fracture near the crack is flatter than the other zones of failure as previously seen in the other annealed parts. A thick irregular oval-shaped inclusion is found on the fracture surface (Fig. 11c). The surface near the boundary of this inclusion contains dimples denoting ductile fracture. The elongated hole recommends that this part has been removed without any breakage of the inclusion. As no inclusion of size as this big was found during the microstructural study, this can be just the separation of smaller dendrites found all over the microstructure in the previous study [19]. Nevertheless, the overall fracture is ductile type as denoted by the dimples shown in Fig. 11d–e. The higher magnification result shows that the dimpled surface
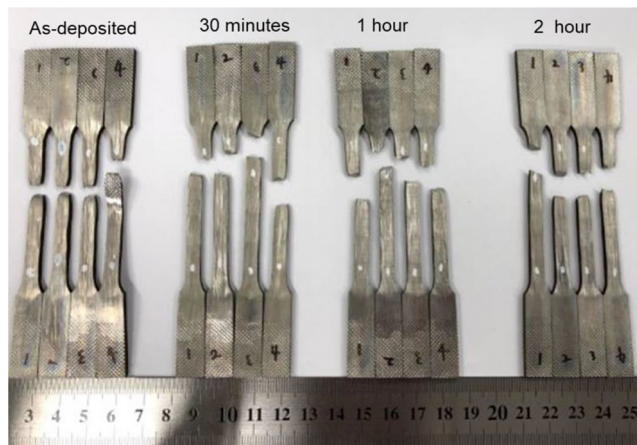
Fig. 7 Inconel 625 as-deposited fractured surface. **a** Fractured surface at low magnification. **b** Spot 1 of (**a**). **c** Higher magnification view of red designated area of (**b**). **d** Higher magnified view of spot 2 of (**a**). Yellow arrows denoting features similar to (**c**)
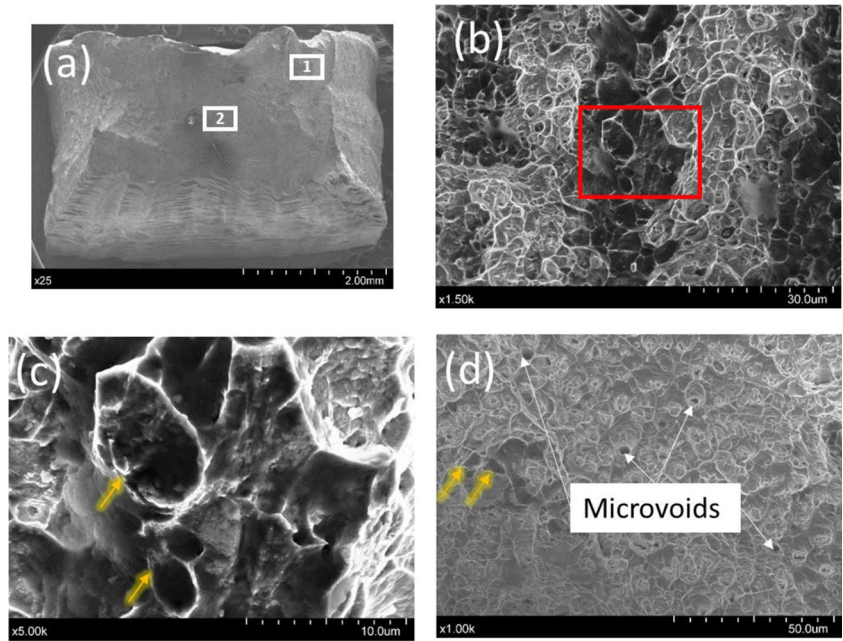
consists of a localized fracture region with a separate nucleus (yellow arrow Fig. 11e). Additionally, there exists an irregular shape on the surface of Fig. 11e (white arrow). These shapes are also found scattered over the fractured surface of the 2-h heat-treated sample. Elemental mapping is carried out to identify these shapes.
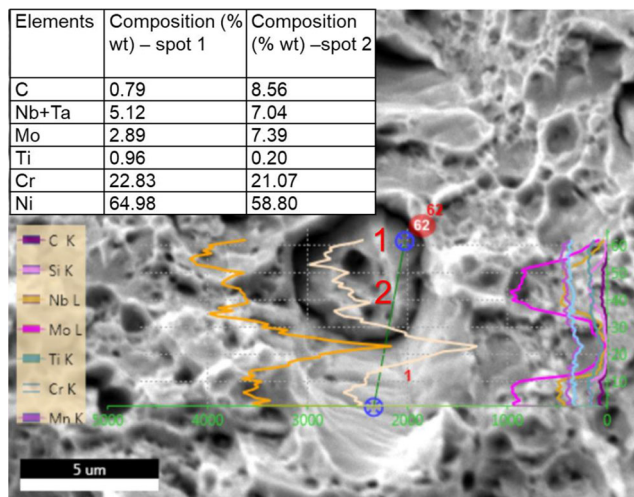

Fig. 8 Fractured surface of a 30-min heat-treated sample. **a** Whole fractured region. **b** Spot 1 on (**a**). **c** Higher magnification micrograph of (**b**). **d** Spot 2. **e** Spot 3. Arrows denoting flat-brittle fracture at some areas. **f** Higher magnification view of designated part of (**e**)
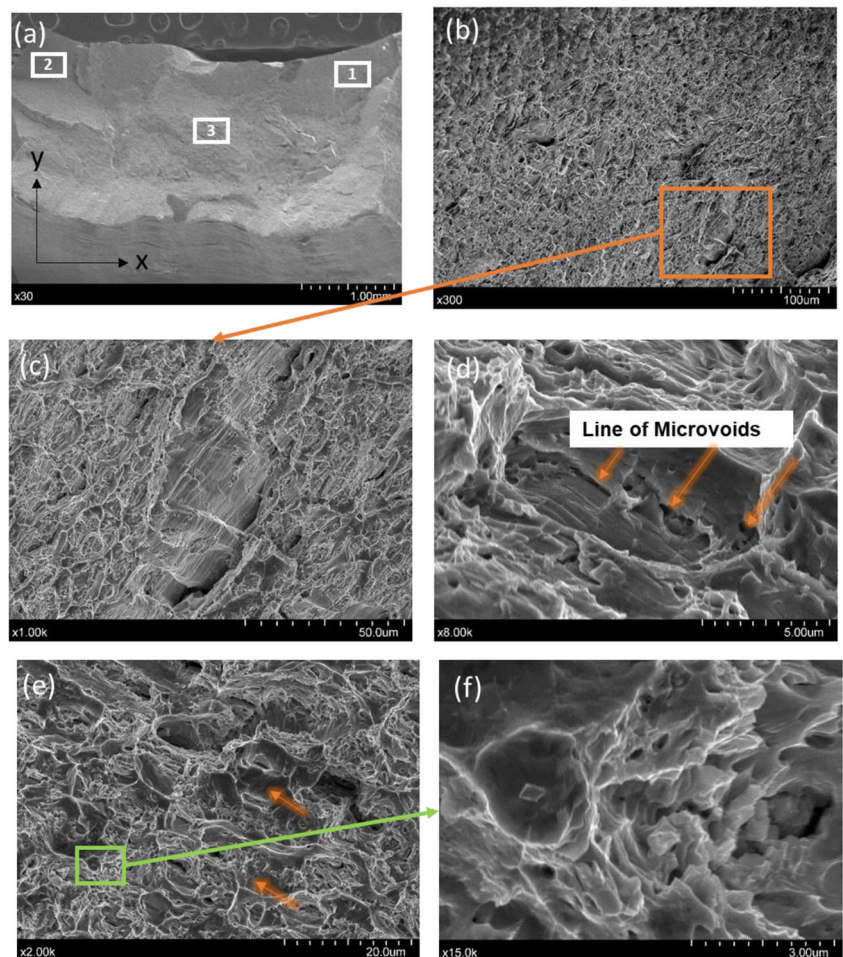
Fig. 9 Fractured surface of 1-h heat-treated sample. **a** Overall fracture zone. **b** Spot 1 of (**a**). **c** High magnification view of (**b**). Orange arrows denoting river patterns. Yellow arrows denoting microvoids. **d** Spot 3. Arrows denoting smooth-shaped unidentified inclusions. **e** Spot 2—arrow denoting an isolated part in the fractography from the surrounding matrix [37]
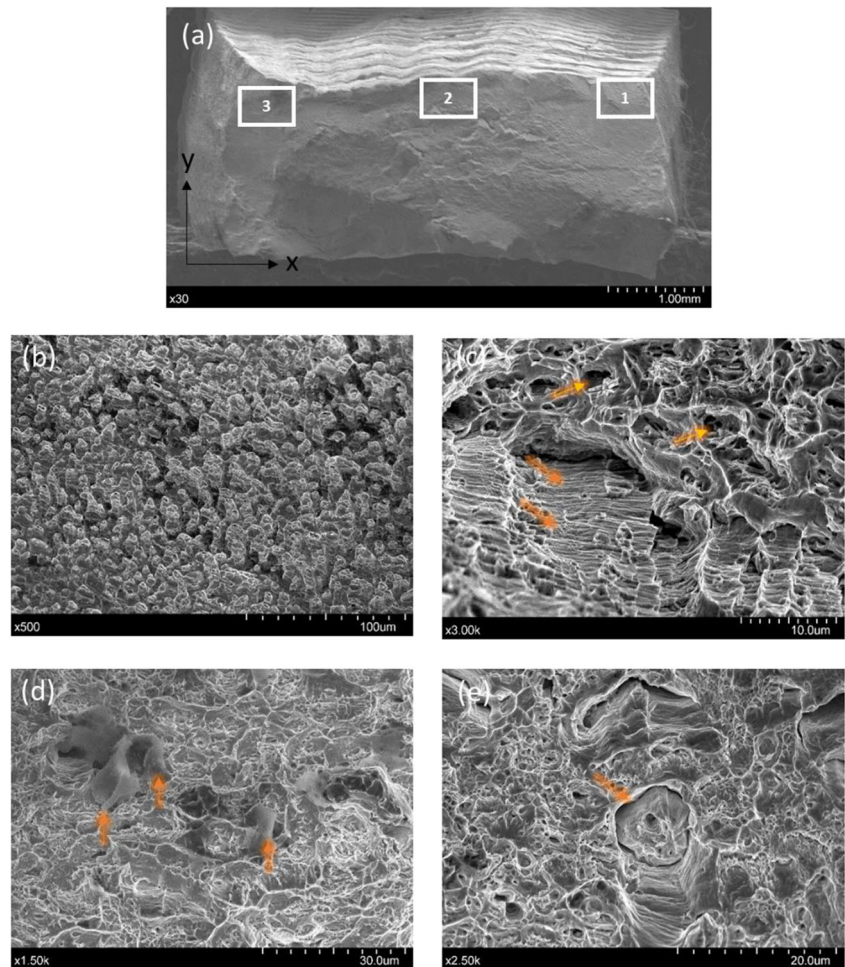
The presence of blocky shapes is more apparent in Fig. 12a. The blocky shapes are mostly present on the dimple boundary and are observed to resist the dimpling process. The elemental map in Fig. 12b–c shows that the blocky shapes

contain more Nb and Ti. In the author's previous study [19], these blocky shapes were denoted as Ti-based MC carbides, which were found only after heat treatment for a longer hold time. Furthermore, these blocky carbides were previously found to resist tensile failure by strengthening the grain boundary in the case of selectively laser-melted Inconel 625 [1]. Therefore, it can be reasonably assumed that these blocky shapes are Ti-based carbides along the grain boundary.

4 Discussion: correlation of mechanical properties, microstructure, and WAAM process

The presence of Laves phases in the microstructure of the as-fabricated sample [19] may have impacted the ultimate tensile strength of WAAMed Inconel 625. Laves phases are responsible for impeding dislocation motion as well as act as a source of crack nucleation zone [39]. This may cause tensile strength to decline. The gradual increase of UTS can also be correlated to the effect of this detrimental phase. With a rising heat treatment time, Laves phases were decreased in the

Elements	Composition (% wt) – spot 1	Composition (% wt) –spot 2
C	0.79	8.56
Nb+Ta	5.12	7.04
Mo	2.89	7.39
Ti	0.96	0.20
Cr	22.83	21.07
Ni	64.98	58.80

Fig. 10 Line scanning along with the possible elongated dendrite group of Fig. 9e
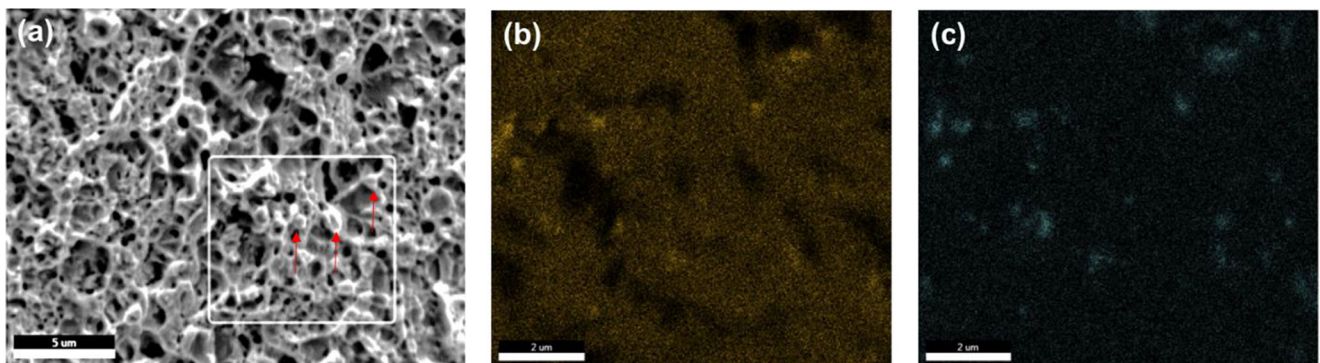
Fig. 11 Fractured surface of 2-h heat-treated sample. **a** Overall fracture zone. **b** Spot 1 of (**a**). arrows denoting granular cracks. **c** Spot 2 of (**a**). The darker oval-shaped area was assumed to be separated as one part. **d** Spot 3. **e** High magnification view of spot 3. White arrow denotes irregular-shaped NbC [37]
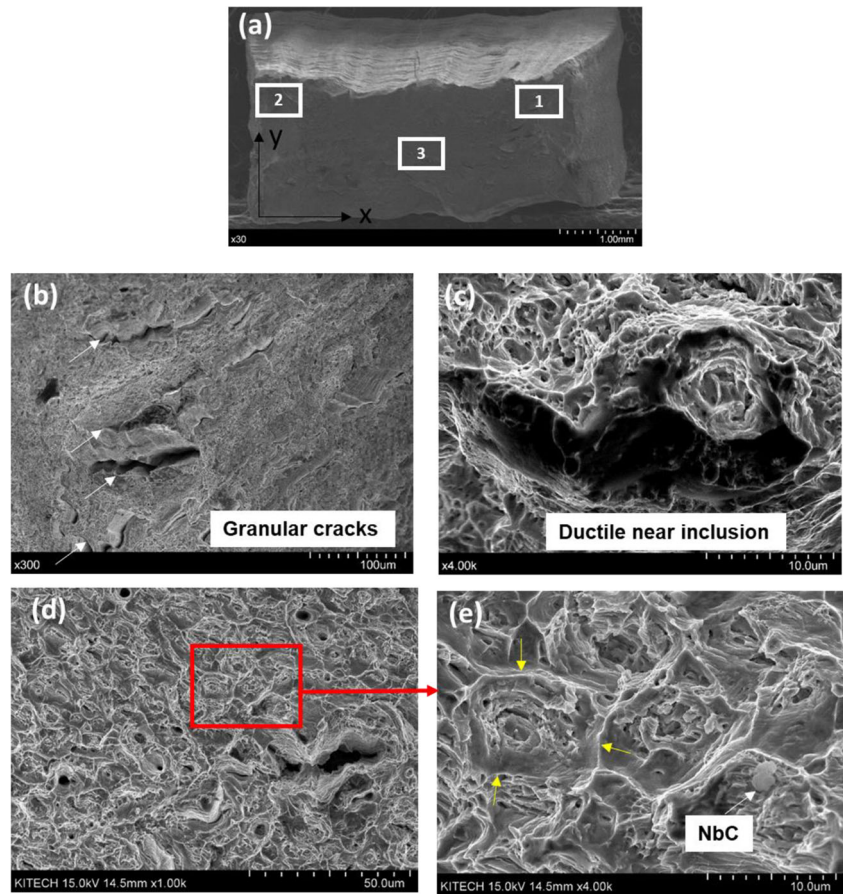
microstructure [19], which may have facilitated a sign of a rise in UTS. However, the fractured surface results may suggest another reason contributing to the increased UTS. The dimples in the fractured surface of the 2-h heat-treated sample contained Ti-based blocky carbides (see Fig. 12 and Section 3.3.4). These particles at the grain boundary may improve the strength by reshaping the grain boundary to a zigzag outline [1]. As Ti-based MC carbides were found in abundance for the 2-h heat treatment case, it can also be a reason for the increased UTS.

The YS remains unchanged after 30-min and 1-h of heat treatment, despite a sign of decline in the average (3–4% decrease). However, 2-h of heat treatment rather provides a sign of increase (6–7% for average YS). The possible reason for this phenomenon can be correlated to two important changes in the microstructure during heat treatment, such as (1) evolution of strengthening elements (Nb & Mo) due to heat treatment and (2) precipitation of secondary phases and their evolution observed in the first part of this study [19]. Strengthening elements were found more dispersed over the microstructure in the as-deposited condition [19]. These

Fig. 12 **a** Blocky particles throughout the fractured surface of the 2-h heat-treated sample. Elemental map of the rectangular area: **b** Elemental map of Nb. **c** Elemental map of Ti

Table 2 CMT-WAAM comparison with other manufacturing methods in terms of mechanical strength

Process		Tensile strength, MPa	Yield strength, MPa	% Elongation, %	References
CMT-WAAM	As deposited	658 ± 4	373 ± 5	56 ± 4	Table 1
	30 min of heat-treated	669 ± 7	363 ± 10	48 ± 2	
	1 h heat treated	672 ± 8	360 ± 11	43 ± 1	
	2 h heat treated	688 ± 4	397 ± 15	46 ± 3	
EBM	As built	750	410	44	Lewandowski and Seifi [42]
	HIP	770	330	69	
Laser powder bed fusion		892	524	54	
Pulsed plasma arc deposition		721	438	49	Xu et al. [15–17]
Laser rapid manufactured		925 ± 12	568 ± 20	46 ± 2	Paul et al. [43]
Gas tungsten arc welded		684 ± 23		40.13 ± 3.7	Wang et al. [14]
Cast		710	350	48	Xu et al. [15–17]
Laser metal deposition		882 ± 7	480 ± 20	36 ± 5	Rombouts et al. [44]
Selective laser melted		900	380	58	Rivera et al. [45]

dispersed particles could anchor the dislocations thereby preventing them to move [40]. The strengthening elements tend to accumulate into smaller particles rather than spreading over the microstructure when heat treatment was employed. Subsequently, secondary phases (δ and MC carbide) start to precipitate from the accumulated clusters of strengthening elements. The amount of δ and MC carbide precipitation gradually increases due to the increased heat-treating hold time (1.26% and 4.30% for the δ phase).

This evolution might have affected the YS in the heat-treated condition. Although, due to loss of strengthening elements, less dislocation could be anchored, the secondary phase precipitation compensates for that. These phases let the dislocations to multiply and entangle which impede dislocation movement again [41]. However, the amount of precipitation may not be enough to compensate for the accumulation of strengthening elements. At 2-h heat treatment, the precipitation gets doubled and the subsequent anchoring of dislocations could compensate for the reduction of strengthening elements. As a result, YS at this point shows a sign of increase than the as-deposited sample.

Table 2 showcases the CMT-WAAM result with other additive manufacturing (AM) methods obtained in previous studies. In the case of UTS, the as-deposited result is lower than all the other AM methods. However, after heat treatment, the UTS has shown a sign of increase which can be investigated in the future for further improvement. Furthermore, the fractography of all the samples although designates predominantly ductile, but areas of different fracture behavior. This proves the presence of high anisotropy in the microstructure as found in the previous study [19]. Nevertheless, YS of the 2-h heat-treated sample is within 10% of most of the AM methods
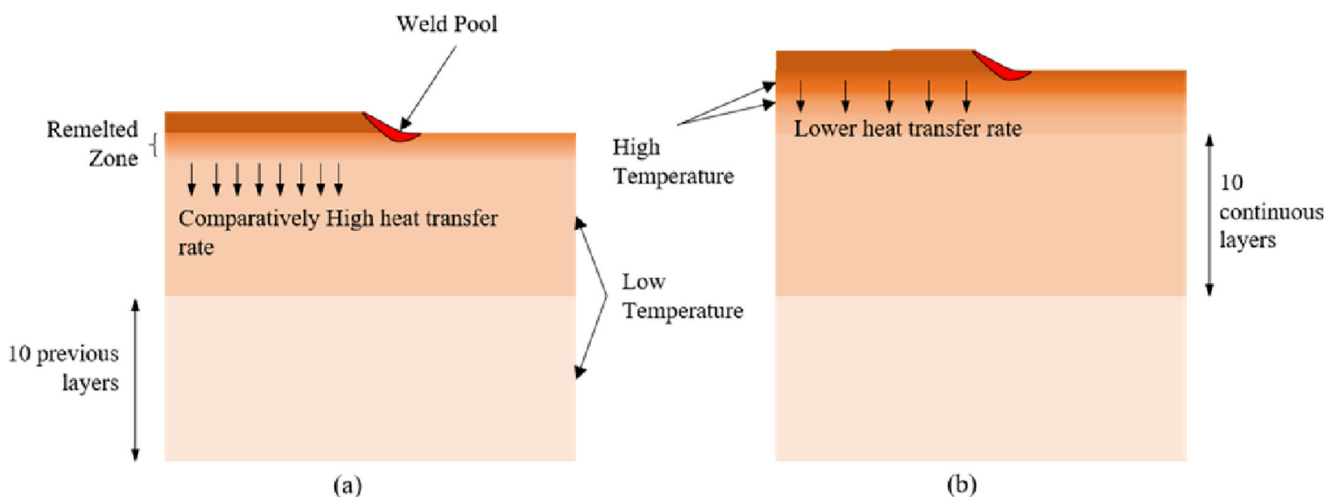
Fig. 13 Different heat transfer mechanisms caused by deposition sequence. **a** Higher heat transfer rate at a new layer deposition right after the interval. **b** Lower heat transfer rate after continuous three-layer depositions

(EBM, PPAD, SLM). The percentage elongation found for the as-deposited CMT-WAAM case is higher than most of the manufacturing processes. Only hot isostatically pressed (HIPed) EBM and as-deposited SLM shows higher elongation than the as-deposited condition for this study.

The heat treatment procedure seems to gradually homogenize the microhardness of the Inconel 625 fabricated by the CMT-WAAM technique. This trend can be either due to the homogenization of phases due to heat treatment. Evidence of higher hardness at the interface of two weld layers is also found in previous studies [18, 46, 47]. A temperature difference-based hypothesis can be formulated for this hardness behavior.

During the deposition, ten metal layers were deposited sequentially which is followed by an interval to cool off the heated layers. The subsequent start of ten deposition then remelt the previous layer and the liquid weld metal at the interface experience a high cooling rate due to the low temperature of the previous layers (Fig. 13a). However, when the deposition continues up to ten layers, the weld metal is deposited on the hot recently solidified metal layers (Fig. 13b). As a result, the cooling rate is lower at the remelted interface of these layers. The faster cooling rate makes the hardness at this point to be higher than the other layer interfaces [46]. However, Yangfan et al. found varying microhardness in Inconel 625 as the result of varying dendrite morphology and density. Therefore, further study with location-specific phase analysis is required to find out the specific reasons behind this behavior.

Overall, the tensile strength of the Inconel 625 fabricated by the CMT-WAAM method is closely related to the secondary phases it contains and the strengthening elements. A process temperature-dependent microhardness behavior is hypothesized which will be studied further in the future.

5 Conclusion and future works

A comprehensive analysis is performed on the mechanical properties of wire + arc additively manufactured Inconel 625 parts. The microstructural study that was previously done is successfully correlated to the mechanical properties. Several significant conclusions can be drawn from this study as follows:

1. The UTS is highest for 2 h of annealing among the heat treatment conditions performed. The ductility and associated yield strength are also comparable with other AM studies for this case. Therefore, the 2-h annealing at 980 °C temperature can be denoted as the best condition for the heat treatment of wire + arc additively manufactured Inconel 625.

2. The microstructural evolution of strengthening elements (Nb and Mo) and precipitation of secondary phases may have controlled the yield strength of the material.

3. The gradual increase of ultimate tensile strength is due to the precipitation and subsequent increase of the δ phases and MC carbides at the grain boundaries.

4. The fractured surfaces designate mostly transgranular type ductile failure of the material. The effect MC carbide on the tensile strength seems to be verified by the fractured surface results. The fractured surface seems to contain deep long cracks in the heat-treated condition. The presence of these cracks may affect the tensile strength of the material which may need further investigation.

5. The average microhardness of the material does not change significantly due to heat treatment. However, location-specific varied microhardness has been observed and needs further study.

Although the material performance is comparable with wire-based additive manufacturing, it needs more investigation to be up to the strength level of powder-based methods. Solution treatment may further increase the strength level of this material and is recommended for future investigation.

References

1. Li S, Wei Q, Shi Y, Zhu Z, Zhang D (2015) Microstructure characteristics of Inconel 625 Superalloy manufactured by selective laser melting. J Mater Sci Technol 31(9):946–952. https://doi.org/10.1016/j.jmst.2014.09.020

2. Yeni C, Koçak M (2008) Fracture analysis of laser beam welded superalloys Inconel 718 and 625 using the FITNET procedure. Int J Press Vessel Pip 85(8):532–539. https://doi.org/10.1016/j.ijpvp.2008.02.004

3. ASTM International (2014a) F3055-14a standard specification for additive manufacturing nickel alloy (UNS N07718) with powder bed fusion. In ASTM Standard ASTM International https://doi.org/10.1520/F3055-14A

4. ASTM International (2014b) F3056-14e1 standard specification for additive manufacturing nickel alloy (UNS N06625) with (Issue 2014). ASTM International https://doi.org/10.1520/F3056-14E01

5. Sciaky Inc (n.d.) Benefits of wire vs. powder metal 3D printing. Retrieved September 24, 2019, from https://www.sciaky.com/additive-manufacturing/wire-vs-powder Accessed 24 Sept 2019

6. Shipley H, McDonnell D, Culleton M, Coull R, Lupoi R, O'Donnell G, Trimble D (2018) Optimisation of process parameters to address fundamental challenges during selective laser melting of Ti-6Al-4V: a review. Int J Mach Tools Manuf 128:1–20. https://doi.org/10.1016/J.IJMACHTOOLS.2018.01.003

7. Koike R, Takemura S, Kakinuma Y, Kondo M (2018) Enhancement of powder supply efficiency in directed energy deposition based on gas-solid multiphase-flow simulation. Procedia CIRP 78:133–137. https://doi.org/10.1016/j.procir.2018.09.061

8. Ahsan MRU, Kim T, Kim, Bong D, Ji C, Park Y-D (2018) A study on the effect of wire composition on welding with gap and offset in cold metal transfer (CMT) GMAW. J Weld Join 36:12–18. https://doi.org/10.5781/jwj.2018.36.5.2

9. Ahsan MRU, Cheepu M, Ashiri R, Kim TH, Jeong C, Park YD (2017) Mechanisms of weld pool flow and slag formation location in cold metal transfer (CMT) gas metal arc welding (GMAW). Weld World 61:1275–1285. https://doi.org/10.1007/s40194-017-0489-y

10. Dutra JC, Gonçalves de Silva RH, Marques C (2015) Melting and welding power characteristics of MIG–CMT versus conventional MIG for aluminium 5183. Weld Int 29:181–186. https://doi.org/10.1080/09507116.2014.932974

11. Selvi S, Vishvaksenan A, & Rajasekar E (2018) Cold metal transfer (CMT) technology - an overview. In Defence Technology (Vol. 14, issue 1, pp. 28–44). Elsevier ltd. https://doi.org/10.1016/j.dt.2017.08.002

12. Cardozo EP, Ríos S, Ganguly S, D'Oliveira ASCM (2018) Assessment of the effect of different forms of Inconel 625 alloy feedstock in plasma transferred arc (PTA) additive manufacturing. Int J Adv Manuf Technol 98(5–8):1695–1705. https://doi.org/10.1007/s00170-018-2340-z

13. Feng Y, Liu J, Wang S, Sun Q, Xu P, Liu Y (2018) Effect of solution treatment on the microstructure of Inconel 625 alloy fabricated by arc additive manufacturing. Trans China Weld Inst 39(6):81–85. https://doi.org/10.12073/j.hjxb.2018390154

14. Wang JF, Sun QJ, Wang H, Liu JP, Feng JC (2016) Effect of location on microstructure and mechanical properties of additive layer manufactured Inconel 625 using gas tungsten arc welding. Mater Sci Eng A 676(October 2017):395–405. https://doi.org/10.1016/j.msea.2016.09.015

15. Xu FJ, Lv YH, Xu BS, Liu YX, Shu FY, He P (2013a) Effect of deposition strategy on the microstructure and mechanical properties of Inconel 625 superalloy fabricated by pulsed plasma arc deposition. Mater Des 45:446–455. https://doi.org/10.1016/j.matdes.2012.07.013

16. Xu F, Lv Y, Liu Y, Shu F, He P, Xu B (2013b) Microstructural evolution and mechanical properties of Inconel 625 alloy during pulsed plasma arc deposition process. J Mater Sci Technol 29(5):480–488. https://doi.org/10.1016/j.jmst.2013.02.010

17. Xu F, Lv Y, Liu Y, Xu B, He P (2013c) Effect of heat treatment on microstructure and mechanical properties of Inconel 625 alloy fabricated by pulsed plasma arc deposition. Phys Procedia 50:48–54. https://doi.org/10.1016/j.phpro.2013.11.010

18. Yangfan W, Xizhang C, Chuanchu S (2019) Microstructure and mechanical properties of Inconel 625 fabricated by wire-arc additive manufacturing. Surf Coat Technol 374:116–123. https://doi.org/10.1016/j.surfcoat.2019.05.079

19. Tanvir ANM, Ahsan MRU, Ji C, Hawkins W, Bates B, Kim DB (2019) Heat treatment effects on Inconel 625 components fabricated by wire + arc additive manufacturing (WAAM)—part 1: microstructural characterization. Int J Adv Manuf Technol 103(9–12):3785–3798. https://doi.org/10.1007/s00170-019-03828-6

20. Lippold JC, Dupont JN, Kiser SD (2009) Welding metallurgy and weldability of nickel-base alloys. J Chem Inf Model 53(9):456. https://doi.org/10.1017/CBO9781107415324.004

21. Lippold JC (2015) Welding metallurgy and weldability. In: Welding Metallurgy and Weldability. Wiley. https://doi.org/10.1002/9781118960332

22. Floreen S, Fuchs GE, & Yang WJ (1994) The metallurgy of alloy 625. Superalloys 718, 625, 706 and Various Derivatives (1994), 13–37. https://doi.org/10.7449/1994/Superalloys_1994_13_37

23. Radavich JF, & Fort A (1994) Effects of long time exposure in alloy 625 at 1200°F, 1400°F and 1600°F. Superalloys 718,625 and Various Derivatives, 635–647

24. Lass EA, Stoudt MR, Williams ME, Katz MB, Levine LE, Phan TQ, Gnaeupel-Herold TH, Ng DS (2017) Formation of the Ni3Nb δ-phase in stress-relieved Inconel 625 produced via laser powder-bed fusion additive manufacturing. Metall Mater Trans A 48:5547–5558. https://doi.org/10.1007/s11661-017-4304-6

25. Liu D, Zhang X, Qin X, Ding Y (2017) High-temperature mechanical properties of Inconel-625: role of carbides and delta phase. Mater Sci Technol (United Kingdom) 33(14):1610–1617. https://doi.org/10.1080/02670836.2017.1300365

26. Cieslak MJ, Headley TJ, Romig AD, Kollie T (1988) A melting and solidification study of alloy 625. Metall Trans A 19(9):2319–2331. https://doi.org/10.1007/BF02645056

27. DuPont JN (1996) Solidification of an alloy 625 weld overlay. Metall Mater Trans A 27(11):3612–3620. https://doi.org/10.1007/BF02595452

28. Silva CC, De Miranda HC, Motta MF, Farias JP, Afonso CRM, Ramirez AJ (2013) New insight on the solidification path of an alloy 625 weld overlay. J Mater Res Technol 2(3):228–237. https://doi.org/10.1016/j.jmrt.2013.02.008

29. Chang K-M, Lai H-J, & Hwang J-Y (1994) Existence of Laves phase in Nb-hardened superalloys. Superalloys 718, 625, 706 and Various Derivatives (1994). https://doi.org/10.7449/1994/Superalloys_1994_683_694

30. Chandler H (1996b) Heat treater's guide: practices and procedures for nonferrous alloys. In ASM International

31. Shankar V, Bhanu Sankara Rao K, Mannan SL (2001) Microstructure and mechanical properties of Inconel 625 superalloy. J Nucl Mater 288(2-3):222–232. https://doi.org/10.1016/S0022-3115(00)00723-6

32. Mu Y, Wang C, Zhou W, Zhou L (2018) Effect of Nb on δ phase precipitation and the tensile properties in cast alloy IN625. Metals 8(2):86. https://doi.org/10.3390/met8020086

33. Marchese G, Lorusso M, Parizia S, Bassini E, Lee JW, Calignano F, Manfredi D, Terner M, Hong HU, Ugues D, Lombardi M, Biamino S (2018) Influence of heat treatments on microstructure evolution and mechanical properties of Inconel 625 processed by laser powder bed fusion. Mater Sci Eng A 729:64–75. https://doi.org/10.1016/j.msea.2018.05.044

34. Chandler H (1996a) ASM handbook: heat Treater's guide-practices and procedures for nonferrous alloys. In ASM International

35. Fang XY, Li HQ, Wang M, Li C, Guo YB (2018) Characterization of texture and grain boundary character distributions of selective laser melted Inconel 625 alloy. Mater Charact 143:182–190. https://doi.org/10.1016/j.matchar.2018.02.008

36. Dinda GP, Dasgupta AK, Mazumder J (2009) Laser aided direct metal deposition of Inconel 625 superalloy: microstructural evolution and thermal stability. Mater Sci Eng A 509:98–104. https://doi.org/10.1016/j.msea.2009.01.009

37. Tanvir ANM (2020) Wire + arc additive manufacturing of high-performance alloys. Tennessee Technological University

38. Das A, Das SK, Tarafder S (2009) Correlation of fractographic features with mechanical properties in systematically varied microstructures of Cu-strengthened high-strength low-alloy steel. Metall Mater Trans A 40:3138–3146. https://doi.org/10.1007/s11661-009-9999-6

39. Manikandan SGK, Sivakumar D, Kamaraj M, Rao KP (2012) Laves phase control in Inconel 718 weldments. Mater Sci Forum 710:614–619. https://doi.org/10.4028/www.scientific.net/MSF.710.614

40. Dislocations and Strengthening Mechanisms (n.d.) Retrieved April 11, 2019, from https://www2.virginia.edu/bohr/mse209/chapter7.htm Accessed 24 Sept 2019

41. Zhang D, Niu W, Cao X, Liu Z (2015) Effect of standard heat treatment on the microstructure and mechanical properties of selective laser melting manufactured Inconel 718 superalloy. Mater Sci Eng A 644:32–40. https://doi.org/10.1016/j.msea.2015.06.021

42. Lewandowski JJ, Seifi M (2016) Metal additive manufacturing: a review of mechanical properties. Annu Rev Mater Res 46(1):151–186. https://doi.org/10.1146/annurev-matsci-070115-032024

43. Paul CP, Ganesh P, Mishra SK, Bhargava P, Negi J, Nath AK (2007) Investigating laser rapid manufacturing for Inconel-625 components. Opt Laser Technol 39(4):800–805. https://doi.org/10.1016/j.optlastec.2006.01.008

44. Rombouts M, Maes G, Mertens M, Hendrix W (2012) Laser metal deposition of Inconel 625: microstructure and mechanical properties. J Laser Appl 24(5):052007. https://doi.org/10.2351/1.4757717

45. Rivera OG, Allison PG, Jordon JB, Rodriguez OL, Brewer LN, McClelland Z, Whittington WR, Francis D, Su J, Martens RL, Hardwick N (2017) Microstructures and mechanical behavior of Inconel 625 fabricated by solid-state additive manufacturing. Mater Sci Eng A 694(March):1–9. https://doi.org/10.1016/j.msea.2017.03.105

46. Nicholas J, & Abson D (2008) The prediction of maximum HAZ hardness in various regions of multiple pass welds. https://www.twi-global.com/technical-knowledge/published-papers/the-prediction-of-maximum-haz-hardness-in-various-regions-of-multiple-pass-welds-june-2008#ref11 Accessed 29 Sept 2019

47. Tanvir ANM, Ahsan MRU, Seo G, Bates B, Lee C, Liaw PK, Noakes M, Nycz A, Ji C, Kim DB (2020) Phase stability and mechanical properties of wire + arc additively manufactured H13 tool steel at elevated temperatures. J Mater Sci Technol. https://doi.org/10.1016/j.jmst.2020.04.085